Dynamical behavior of electrified pendant drops

C. Ferrera[1], J. M. López-Herrera[2], M. A. Herrada[2], J. M. Montanero[1], and A. J. Acero[1]

(1) Depto. de Ingeniería Mecánica, Energética y de los Materiales,

Universidad de Extremadura, E-06006 Badajoz, Spain,

(2) Depto. de Ingeniería Aeroespacial y Mecánica de Fluidos,

Universidad de Sevilla, E-41092 Sevilla, Spain

(Dated: September 11, 2012)

Abstract

The electrohydrodynamic response of low-conductivity pendant drops to a step change in the electric field magnitude was examined both numerically and experimentally. Both the leaky-dielectric and perfect-conductor models were solved in the simulations. Experiments were conducted to precisely measure the drop interface shape as a function of time. The drop oscillated for applied voltages smaller than a critical value which depended on the rest of governing parameters. It stretched and subsequently emitted a microjet from its tip for electric potentials above that critical value. The perfect-conductor model described accurately the oscillations of subcritical drops. This model also provided satisfactory results for the prejetting regime in the supercritical case. We found a good agreement between the leaky-dielectric model and the experiments for the drop-jet transitional region, despite the fact that the tip streaming arose on a time scale much shorter than the electric relaxation time. This result shows the capability of the leaky-dielectric model to describe the flow in this singular region. The numerical simulations allowed us to describe the pressure and velocity fields in the transitional region.

I. INTRODUCTION

The understanding of the effects produced by electric fields on capillary systems is of great importance in a number of applications including inkjet printing, spring coating, electrowetting, mass spectrometry, fabrication of microspheres of biological materials, direct handling of living cells, etc. In drop-on-demand atomization techniques, electrically charged drops are produced in a controlled manner from liquid menisci periodically formed and stretched by electric forces until they are completely or partially ejected[1,2]. The so-called cone-jet mode of electrospray[1,3–6] is a very useful atomization technique to produce steadily a variety of capillary shapes with sizes ranging from hundreds of microns down to a few nanometers[1,4,5].

Many electrohydrodynamic phenomena arising in both periodic and steady flows have been studied both theoretically and experimentally over the last decades. Low-conductivity liquids, such as ionic solutions, are commonly considered in those studies. In this case, the electrical conductivity is assumed to be high enough for the free charges to migrate from the bulk to the interface on a time scale much shorter than the hydrodynamic times characterizing the global behavior of the system. Nevertheless, the conductivity is sufficiently low for inner electric fields to appear under certain conditions[7]. The existence of charges in the interface and a non-zero inner electric field gives rise to the appearance of shear stresses at the liquid free surface (the leaky-dielectric behavior[7]), which feed complex flow patterns. For instance, recirculation cells arise in the tapering menisci formed in the electrospray cone-jet mode for sufficiently low liquid flow rates. These cells are driven by electric shear stresses over the meniscus free surface[8]. Collins *et al.*[9] nicely showed from numerical simulations of the leaky-dielectric model[7] that these stresses drive the tip streaming appearing in a liquid film deformed by electric forces. In this case, the local capillary time characterizing the tip dynamics becomes much shorter than the electric relaxation time, the electric charges do not move over the interface fast enough to screen the external electric field, and important axial electric forces arise on the inner side of the interface. These forces give rise to the shear stresses that power the tip streaming.

Electrified drops have been frequently studied over the past few decades due in large part to their close relationship with both drop-on-demand and steady-flow atomization techniques. The action of electric fields on drops produces a variety of interesting phenomena, such as drop deformation and rotation, breakup and coalescence, and liquid ejection, among

others. The static deformation of floating, pendant, and sessile drops exposed to electric forces has been studied over the last decades[10–12]. There is also a considerable body of literature dealing with the dynamic response of drops to oscillatory electric fields (see, e.g., Refs.[13,14] and references therein). The impulsive motion of a pendant drop due to a step change in the electric field magnitude is closely related to drop-on-demand electrospray atomization techniques, and the transient regimes[2,15] of the cone-jet mode[15,16]. For relatively low values of the applied voltage, the drop deforms following an extensional/oscillatory motion to reach a more elongated shape. If the electric field magnitude exceeds a certain critical value, the pendant drop ejects a liquid ligament from its tip. This ejection can be sustained over time if liquid is injected at an appropriate flow rate, which yields the steady cone-jet mode. The dynamic deformation of both subcritical and supercritical highly conducting drops due to a step change in the electric field magnitude has been examined numerically by Notz and Basaran[17]. Reznik *et al.*[18,19] studied both theoretically and experimentally the response of conductor[18] and low-conductivity compound[19] drops. The numerical results for the subcritical Stokes regime showed an exponential decay to the steady drop shape. The analysis of the drop-jet transitional region indicated that drops behaved as perfect conductors in most of the prejetting regime even for low electric conductivities.

In this paper, we aim at analyzing both numerically and experimentally the electrohydrodynamic response of low-conductivity pendant drops to a step change in the electric field magnitude. Both the leaky-dielectric and perfect-conductor models are considered. The leaky-dielectric model is integrated with a Volume-of-Fluid (VoF) method, while the perfect-conductor approximation is solved by using a spectral collocation technique proposed in this paper. Precise experimental results for the interface shape are obtained from the combination of optical imaging and super-resolution image processing techniques[20]. Both the simulations and experiments show that the drop oscillates if the applied voltage is smaller than a critical value which depends on the rest of governing parameters, while it elongates and expels a microjet from its tip in the supercritical case. The damping rate and frequency characterizing the oscillations of subcritical drops are calculated and measured. The results show that the perfect-conductor model describes accurately those oscillations. This model also provides reasonably good results for the prejetting regime in the supercritical case. Our experimental results for the tip streaming are consistent with the scenario described by Collins *et al.*[9] for electrified films. There is a good agreement between the VoF and

experimental results for the drop-jet transitional region, which shows the capability of the leaky-dielectric model to describe the flow in this singular region. The pressure and velocity fields in the transitional region are analyzed from the simulations, which allows us to gain insight into the physical mechanisms driving the microjet emission.

The paper is organized as follows. The problem is formulated in Sec. II. We present the theoretical models and numerical methods in Sec. III, while the experimental procedure is described in Sec. IV. In Sec. V, the results are showed and discussed. The paper closes in Sec. VI with some concluding remarks.

II. FORMULATION OF THE PROBLEM

Figure 1 shows a sketch of the fluid configuration considered in this work. A drop of volume $\mathcal{V}$ hangs from a circular plate of radius R_0 much greater than the radius R of the triple contact line. This line is assumed to remain at rest at any times. Another circular plate of the same radius R_0 is located concentrically in front of the upper plate at a distance H. The fluid configuration is axisymmetric because the gravity force per unit mass $\mathbf{g}$ acts along the common axis of the parallel plates. The drop behavior depends on the liquid density ρ, viscosity μ, electric conductivity K, and permittivity ε, as well as on the surface tension γ of the interface. The liquid is surrounded by a gas of density ρ_g and viscosity μ_g. The gas is supposed to be an electric insulator with an electric permittivity ε_0 equal to that of vacuum. For $t < 0$, the two plates are kept at the same voltage, and thus the pendant drop is at equilibrium. A constant voltage difference V is applied between the two electrodes for $t \geq 0$. We aim at describing the dynamical response of the pendant drop to this electric pulse.

III. THEORETICAL MODELS AND NUMERICAL METHODS

We present in this section the theoretical models and numerical methods used to analyze the problem formulated in Sec. II. Equations were made dimensionless by using as charaterisitc quantities the triple contact line radius R, the liquid density ρ, the surface tension γ, and the applied voltage V.

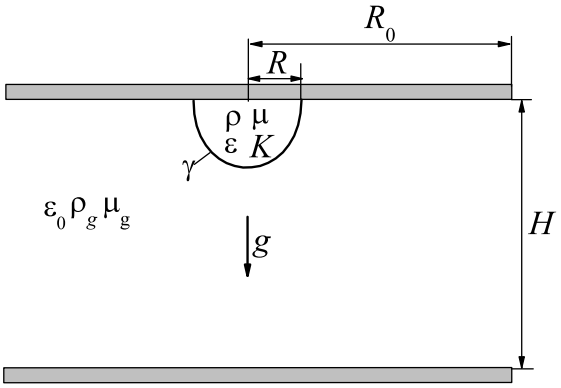

FIG. 1: Sketch of the fluid configuration considered in this work.

A. The leaky-dielectric model and the VoF method

The leaky-dielectric model[7] as applied to our problem can be described as follows. One starts with the incompressible Navier-Stokes equations

$$\nabla \cdot \mathbf{v} = 0, \tag{1}$$

$$\frac{D\mathbf{v}}{Dt} = -\nabla p - \frac{1}{2} B_e \mathbf{E} \cdot \mathbf{E} \nabla \varepsilon_r + B_e \nabla \cdot (\varepsilon_r \mathbf{E}) \mathbf{E} + C \nabla^2 \mathbf{v} \ , \tag{2}$$

for the velocity $\mathbf{v}(\mathbf{r}, t)$ and reduced pressure $p(\mathbf{r}, t)$ fields in both the liquid and gas domains, as well as the Maxwell electrostatic equations

$$\nabla \cdot (\varepsilon_r \mathbf{E}) = \rho_e \ , \quad \nabla \times \mathbf{E} = 0 \ , \tag{3}$$

for the electric field $\mathbf{E}(\mathbf{r}, t)$ in the two domains and for the dimensionless volumetric charge density $\rho_e(\mathbf{r}, t)$ in the drop. In the above equations, $C = \mu(\rho\gamma R)^{-1/2}$ and $B_e = \varepsilon_0 V^2/(R\gamma)$ are the Ohnesorge and electric Bond numbers, respectively, whilst $\varepsilon_r = \varepsilon/\varepsilon_0$ is the relative permittivity. If one neglects both migration of electrical charges due to thermal difussion and net production of positive/negative charges owing to electrochemical reactions, then the conservation equation for the volumetric charge density $\rho_e(\mathbf{r}, t)$ becomes[21]

$$\frac{D\rho_e}{Dt} = \nabla \cdot (-\hat{K} \mathbf{E}) \ , \tag{4}$$

where $\hat{K} = [\rho R^3 K^2/(\gamma \varepsilon_0^2)]^{1/2}$ is the dimensionless electrical conductivity.

The above equations must be integrated considering the kinematic compatibility boundary condition

$$\frac{\partial f}{\partial t} + \mathbf{v} \cdot \nabla f = 0 \ , \tag{5}$$

and the balance of both normal and tangential mechanical and Maxwell stresses on the two sides of the interface

$$\mathbf{t} \cdot ||\tau|| \cdot \mathbf{n} + \mathbf{t} \cdot ||\tau_{\mathbf{M}}|| \cdot \mathbf{n} = 0 \, , \tag{6}$$

$$\mathbf{n} \cdot ||\tau|| \cdot \mathbf{n} + \mathbf{n} \cdot ||\tau_{\mathbf{M}}|| \cdot \mathbf{n} + ||p|| + B(\hat{\mathbf{g}} \cdot \mathbf{r}) - \kappa = 0 \, . \tag{7}$$

The equation $f(\mathbf{r}_s, t) = 0$ determines the interface position $\mathbf{r}_s$, τ and $\tau_{\mathbf{M}}$ stand for the viscous and Maxwell stresses, respectively, $B = (\rho - \rho_g) g R^2/\gamma$ is the gravitational Bond number, and κ is the interface curvature. In addition, $||A||$ denotes the difference between the values taken by the quantity A on the two sides of the interface.

Non-slip boundary conditions and fixed voltage values are prescribed at the electrodes. Regularity conditions are imposed at the symmetry axis, while zero velocity and a linear voltage distribution are set on the outer lateral surface of the numerical domain. The set of equations is completed by considering the equilibrium state corresponding to zero applied voltage for $t = 0$.

One has not as yet made the fundamental approximation leading to the leaky-dielectric model[7]. In this model, one assumes that all characteristic times of hydrodynamic nature are much longer than the electrical relaxation time. Therefore, the volumetric charge density ρ_e is assumed to be zero, and electrical charges are only allowed to exist at the interface. This implies that the volumetric electric forces vanish in the bulk (provided that the electric permittivity ε takes an uniform value), and the electric conductivity can be regarded as a constant.

We performed numerical simulations of the problem formulated in Sec. II by using the VoF method Gerris[22], which has been improved and extended to study electrohydrodynamic flows[21,23]. This method can be regarded as a direct numerical simulation of the leaky-dielectric model[7]. It must be noted that the VoF method treats immiscible fluids as a single one with spatially varying properties through the interface. Therefore, the interface boundary conditions can not be explicitly considered. The surface tension stress is modeled as a volumetric force using the Continuum-Surface-Force approach[24]. The Maxwell stresses are accounted for from the corresponding electric and polarization volumetric forces in the vicinity of the interface. The calculation of these forces relies on the knowledge of the electric charge distribution in this region. To calculate this distribution, the VoF method solves the conservation equation (4) for the volumetric charge density $\rho_e(\mathbf{r}, t)$ with a constant electric

conductivity. The method simulates a "transitory stage" (not interesting for our purposes) that converges to a "leaky-dielectric regime" in which electric charges are confined in a very thin layer next to the interface. The charge migration from the bulk to the interface occurs on a time scale much shorter than any hydrodynamic characteristic time, and thus one can assume that the drop evolution corresponds to that predicted by the leaky-dielectric model for any time. More details of the method can be found elsewhere[21,23]. The solution of the leaky-dielectric model as applied to our problem is obtained as a function of the governing parameters B, B_e, C, $\hat{K}$, and the dimensionless volume $\hat{\mathcal{V}} = \mathcal{V}/R^3$.

In the simulations performed to describe the drop deformation, the minimum cell size was 4.88×10^{-3} (9.76 μm for our experimental configuration). This parameter was decreased down to 3.05×10^{-4} (610 nm for our experimental configuration) to analyze the pressure and velocity fields in the tip streaming of supercritical drops. In this latter case, the algorithm converged to the sought solution in about 3 hours running on an Intel Xeon(R) X5670@2.93Ghz processor.

B. The perfect-conductor model and the spectral collocation method

The perfect-conductor model was also used in this work to describe the oscillations of subcritical drops and the prejetting regime in the supercritical case. In this model, the electric potential is assumed to take the constant value V in the whole drop. In addition, dynamic effects of the surrounding gas are neglected (ρ_g/ρ and $\mu_g/\mu \ll 1$). Use is made of the spherical coordinates (r, θ, ϕ) (Fig. 2) to simplify the formulation. Because the problem is axisymmetric with respect to the axis $\theta = 0$, the liquid and gas integration domains are $(0 \leq r \leq F(\theta, t), 0 \leq \theta \leq \pi/2)$ and $(F(\theta, t) \leq r \leq H, 0 \leq \theta \leq \pi/2)$, respectively. Here, $r = F(\theta, t)$ is the radial position of the drop's free surface, while $r = H$ is the outer boundary (H is the distance between the two parallel plates in the analyzed configuration).

The incompressible Navier-Stokes equations for the liquid velocity $\mathbf{v}(r, \theta; t)$ and reduced pressure $p(r, \theta; t)$ fields are

$$\frac{w_\theta}{r} + u_r + \frac{2u}{r} + \frac{w \cot\theta}{r} = 0 \,, \tag{8}$$

$$u_t + u u_r + \frac{w u_\theta}{r} - \frac{w^2}{r} = -p_r + C\left[u_{rr} + \frac{2u_r}{r} + \frac{u_{\theta\theta}}{r^2} + \frac{\cot\theta u_\theta}{r^2}\right] \,, \tag{9}$$

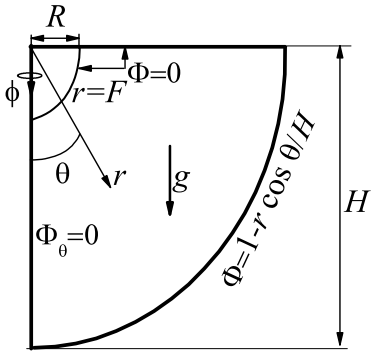

FIG. 2: Integration domain and boundary conditions.

$$w_t + uw_r + \frac{ww_\theta}{r} - \frac{wu}{r} = -\frac{p_\theta}{r} + C\left[w_{rr} + \frac{2w_r}{r} + \frac{w_{\theta\theta}}{r^2} + \frac{\cot\theta w_\theta}{r^2} - \frac{w}{r^2\sin^2\theta}\right] , \qquad (10)$$

where u/w is the radial/meridional velocity component. The subscripts r, θ, and t denote the partial derivatives with respect to the corresponding variables. In addition to the Navier-Stokes equations, one has to integrate the Laplace equation

$$\Phi_{rr} + \frac{2\Phi_r}{r} + \frac{\Phi_{\theta\theta}}{r^2} + \frac{\cot\theta\Phi_\theta}{r^2} = 0 \qquad (11)$$

for the gas electric potential $\Phi(r,\theta;t)$.

Equations (8)-(11) must be integrated with the appropriate boundary conditions. The kinematic compatibility and equilibrium of tangential and normal stresses at the interface $r = F(\theta,t)$ yield

$$F_t + \frac{wF_\theta}{r} - u = 0 , \qquad (12)$$

$$\tau_t = 0 , \qquad (13)$$

$$\tau_n + \frac{1}{2}B_eE_n^2 + p + BF\cos\theta - \kappa = 0 , \qquad (14)$$

where

$$\tau_t = \frac{C}{1+a^2}\left[2au_r - 2a\left(\frac{w_\theta}{F} + \frac{u}{F}\right) + (1-a^2)\left(w_r - \frac{w}{F} + \frac{u_\theta}{F}\right)\right] , \qquad (15)$$

$$\tau_n = -\frac{C}{1+a^2}\left[2u_r + 2a^2\left(\frac{w_\theta}{F} + \frac{u}{F}\right) - 2a\left(w_r - \frac{w}{F} + \frac{u_\theta}{F}\right)\right]$$

are the tangential and normal components of the viscous stresses, respectively, and $a \equiv F_\theta/F$. Besides, the interface curvature κ and the gas electric field E_n at the interface are

$$\kappa = \frac{2}{F\sqrt{1+a^2}} - \frac{F_{\theta\theta}F - F_\theta^2}{(1+a^2)^{3/2}F^3} - \frac{F_\theta\cot\theta}{F^2\sqrt{1+a^2}} , \qquad (16)$$

$$E_n = \frac{F_\theta \Phi_\theta - F\Phi_r}{F\sqrt{1+a^2}} \ . \tag{17}$$

Note that the electric tangential stress is zero because the liquid is assumed to be equipotential. Non-slip $u = w = 0$ and regularity $w = u_\theta = \Phi_\theta = F_\theta = 0$ boundary conditions are imposed both at the solid surface $\theta = \pi/2$ and the symmetry axis $\theta = 0$, respectively. The Laplace equation (11) is solved with the boundary condition $\Phi = 1$ at the upper plate surface $\theta = \pi/2$ and the interface $r = F(\theta, t)$, while the condition $\Phi = 1 - r\cos\theta/H$ is prescribed at the outer boundary $r = H$. The anchorage condition $F(\pi/2, t) = 1$ for the triple contact line is also considered. The set of model equations is completed by considering the equilibrium state corresponding to zero applied voltage for $t = 0$. In our calculations, the dimensionless volume $\hat{\mathcal{V}}$ is regarded as an input parameter, and thus the integral condition

$$\hat{\mathcal{V}} = \int_0^{\pi/2} F^3 \ \sin\theta \ d\theta \tag{18}$$

must be verified. The integration of the above equations provides the velocity $\mathbf{v}(r, \theta; t)$ and reduced pressure $p(r, \theta; t)$ fields in the liquid domain, the gas electric potential $\Phi(r, \theta; t)$, and the drop shape $F(\theta, t)$ as a function of the set of control parameters $\{B,\ B_e,\ C,\ \hat{\mathcal{V}}\}$.

A numerical method is proposed in this work to solve the perfect-conductor model. A boundary-fitted coordinate system[25] was used to calculate the solution. Both the liquid and gas domains were mapped onto the fixed rectangular domain ($0 \le \eta^{l,g} \le 1, 0 \le \xi \le \pi/2$) by means of the coordinate transformations ($\eta^l = r/F, \xi = \theta$) and ($\eta^g = (r-F)/(H-F), \xi = \theta$) for the liquid and gas domains, respectively. The two resulting rectangles were discretized using $n_\eta^l = 12$, $n_\eta^g = 31$, and $n_\xi = 25$ Chebyshev collocation points[26] along the η^l, η^g, and ξ axes, respectively. The (implicit) time advancement is performed using second-order backward finite differences with a time step $\Delta t = 0.05$. The resulting set of $(3n_\eta^l + n_\xi)n_\eta^g + n_\xi$ nonlinear equations for each instant was solved using the iterative Newton-Raphson method implemented in the MATLAB subroutine FSOLVE. The initial guess for the iterations at each time step was the solution for the previous instant.

IV. EXPERIMENTAL METHOD

Experiments were conducted with the configuration sketched in Fig. 3. It consisted of two parallel circular electrodes of radius $R_0 = 5$ cm made of stainless steel. A copper disk of radius $R = 2$ mm and thickness $h = 0.7$ mm was attached to the upper electrode. This

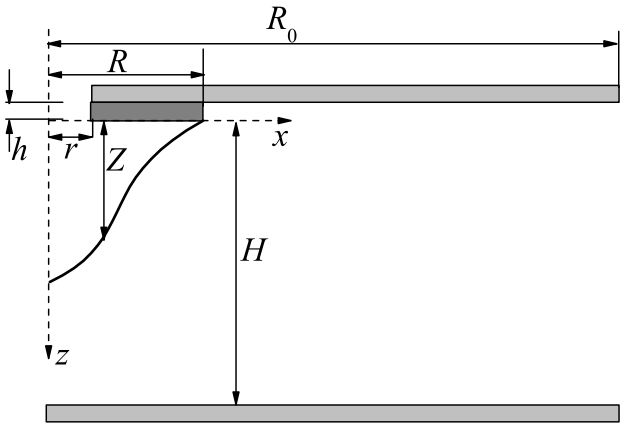

FIG. 3: Experimental configuration.

element was not present in the fluid configuration considered in this work (Fig. 1). It was introduced to ensure the anchorage of the triple contact line. Both the upper electrode and the disk had a circular orifice of radius $r = 0.1$ mm at their centers. The disk was separated from the lower electrode by a distance $H = 10$ mm. A drop of volume $\mathcal{V}$ hung from the disk surrounded by air. A constant voltage V was applied to the upper electrode at $t = 0$, while the lower electrode was kept at ground potential.

The working liquid was 1-octanol (PANREAC) with density $\rho = 824$ kg/m^3, viscosity $\mu = 0.00889$ kg/ms, electrical conductivity $K = 9 \times 10^{-7}$ S/m, and relative permittivity $\varepsilon = 10.3$. The surface tension γ was measured in each experiment with the TIFA method[27] to take into account the slight influence of impurities on its value. The liquid's electrical conductivity K was measured by applying a voltage difference between the ends of a cylindrical borosilicate capillary full of the working liquid, and then measuring the resulting electric current. The rest of the liquid properties were taken from the manufacture's specifications.

Figure 4 shows the apparatus used in the experiments. The experimental cell (A) that contained the two electrodes and the disk was situated horizontally on a goniometer (B). An electric potential V was applied to the upper electrode with a standard DC high voltage power supply (BERTAN 205B-10R) (C), while the lower electrode was connected to ground. A fast-connection switch (D) located between the upper electrode and the voltage power supply allowed the upper electrode to reach the voltage prescribed value much faster than any electrohydrodynamic process. The drop was formed in the open air by injecting liquid with a syringe pump (KDS-270) through the small hole located in the center of the upper

electrode. Digital images were acquired at 28 000 frames per second with an ultra-high-speed camera (PHOTRON, FASTCAM SA5) (E) equipped with optical lenses (OPTO-ENGINEERING TC 2309) (F) providing a frame covering an area of about 6.43×14.47 mm. The camera could be displaced both horizontally and vertically using a triaxial translation stage (G) to focus the drop. The fluid configuration was illuminated from the back side by cool white light provided by an optical fiber (H) connected to a light source. A frosted diffuser (I) was positioned between the optical fiber and the drop to provide uniform lighting. To check that the drop anchored perfectly to the disk edge, we also acquired images of the configuration by using an auxiliary CCD camera (not shown in Fig. 4) with an optical axis perpendicular to that of the main camera. All these elements were mounted on an optical table (J) with a pneumatic anti-vibration isolation system (K) to damp the vibrations coming from the building.

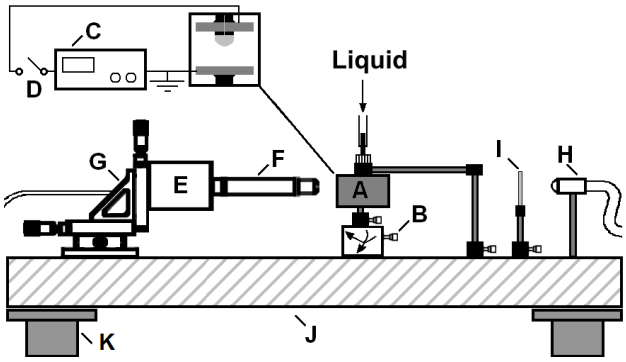

FIG. 4: Experimental apparatus consisting of the following elements: experimental cell (A), goniometer (B), DC high voltage power supply (C), fast-connection switch (D), digital camera (E), optical lenses (F), triaxial translation stage (G), optical fiber (H), frosted diffuser (I), optical table (J), and pneumatic anti-vibration isolation system (K).

A. Experimental procedure

In each experimental run, a pendant drop of the desired volume was formed by injecting liquid between the two electrodes. We let the drop age for five minutes. During this period of time, the surface tension decreased slightly due to the free surface contamination until reaching a constant value. A drop image was acquired at the end of this process to determine

the surface tension value with the TIFA method[27]. Then, the voltage power supply was switched on. After several seconds, the fast-connection switch was turned on. Images of the pendant drop were acquired starting just before the switch was turned on, and ending when the drop reached a new equilibrium state or broke up. The images were processed (as will be described in Sec. IV B) to measure the instantaneous position $Z(x)$ of the free surface contour. Here, Z is the vertical distance between a free surface element and the disk for a horizontal distance x from the disk center (see Fig. 3). This result allowed us to calculate the triple contact line radius and drop volume as a function of time. We verified that those values remained constant over the whole drop evolution.

B. Image processing technique

Here, we shall briefly describe the main aspects of the image processing technique used to precisely determine the free surface position. Details of the method can be found elsewhere[20,28]. The contours of the free surface in the image were detected using a two-stage procedure. In the first stage, a set of pixels probably corresponding to the contour being sought was extracted using Canny's method[29]. The accuracy of Canny's method is limited to the pixel size. In the second stage, the accuracy of the detected contours was improved to the sub-pixel level by analyzing the gray intensity profile along the direction normal to the contour. Fitting the sigmoid (Boltzmann) function[30] to the gray intensity values allowed us to obtain a continuous function in the transient region of the gray profile. The contour point was found by applying the local thresholding criterion. The number of resulting contour points was approximately equal to the number of pixels of the image along the vertical direction. Once the drop contour had been detected, it was rotated to its vertical position (the rotation angle was less than 0.3° in all the cases analyzed). Finally, it was smoothed with the Savitzky-Golay method[31].

By way of illustration, Fig. 5 shows an image of a supercritical drop acquired just after the jet emission. The graphs show the detected position of the free surface. The image processing technique managed to provide a smooth contour even for the drop tip, whose diameter was of the order of one pixel size. The jet base had a nearly conical shape with a vertical semi-angle of about 31°, similar to that observed in numerical simulations[18].

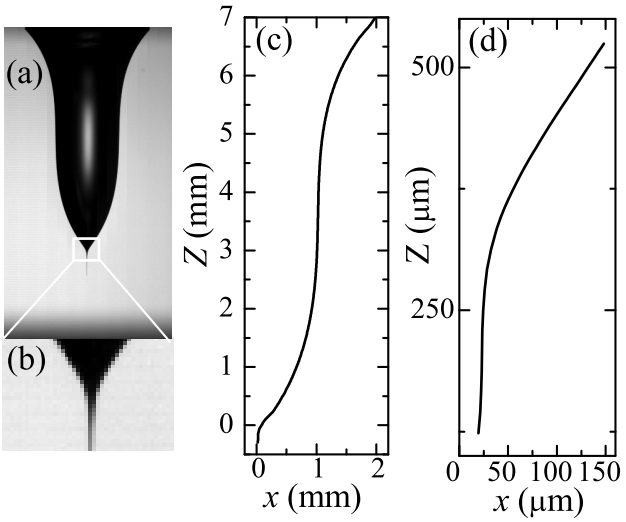

FIG. 5: Deformation of a supercritical drop of volume $\mathcal{V} = 26.05$ mm^3 subject to a voltage difference $V = 4000$ V just after emitting a microjet from its tip. The photographs are images of the entire drop (a) and its tip (b). The graphs show the free surface position of the entire drop (c) and its tip (d).

V. RESULTS

The configuration considered in the simulations differed slightly from that examined in the experiments mainly due to the presence of the disk in the experimental configuration (see Figs. 1 and 3). That element was introduced in the experimental configuration to force the triple contact line to anchor to a fixed position (the disk edge). We did not include the disk in the numerical calculations because of the difficulty of adapting the grid of collocation-technique points to that geometrical detail. In order to assess the validity of this simplification, we compared the numerical and "experimental" electric field distributions at the drop free surface. The experimental distribution was obtained by the finite element solver COMSOL for an equipotential drop at equilibrium with the free surface contour measured in one of our experiments (COMSOL does not solve the coupled electro- and hydro-static problems). The discrepancy between the numerical and experimental electric field distributions was found to be small. The maximum value of the experimental distribution was about 7% larger than that of the numerical distribution. This may explain slight deviations of the theoretical predictions with respect to the experimental results. In fact, the

voltages (electric Bond numbers) considered in the spectral technique were slightly different from the experimental ones to match the free surface deformations.

A. Subcritical drops

A subcritical pendant drop undergoes the following three processes when the switch is turned on: (i) a voltage drop is established between the two parallel electrodes, (ii) electric charges are transferred to the free surface and accumulate there, and (iii) the liquid flows until a new equilibrium shape is reached. The resistance-capacitance time t_{RC} and the charge relaxation time $t_K \equiv \varepsilon/K$ that characterize the first and second processes, respectively, are much shorter than any characteristic hydrodynamic time of the problem. Thus, the migration of free electric charges to the free surface can be regarded as instantaneous as compared with the drop evolution. As the drop deforms, the electric charges accumulated in the free surface move over that surface to screen the external electric field. This process also takes place on a time scale much shorter than that given by any hydrodynamic time. Therefore, the electric field inside the droplet vanishes for any time, and thus the liquid polarization forces can be neglected.

The liquid flow in the equipotential drop is originated by the appearance of electric stresses at the free surface. Both the electric charge density and the electric stress reach their maximum values at the apex. The electric stress is balanced by the hydrostatic and capillary pressures (viscous stresses normal to the free surface can be generally neglected). Therefore, the reduced pressure decreases at the apex, and the liquid is suctioned towards that region. This liquid motion stretches the drop, increasing the free surface curvature at the apex. Consequently, a restoring capillary force appears in that region. If the electric stresses are not high enough to overcome the surface tension force, then the drop reaches a new equilibrium state.

The drop's evolution towards the equilibrium state is governed by the liquid dynamic properties. The time scale on which the drop reaches its new equilibrium shape can be determined by establishing a balance between the viscous stress $\mu\partial^2\tilde{w}/\partial z^2 \sim \mu v_c/R^2$ and the axial inertia term $\rho d\tilde{w}/dt \sim \rho v_c/t_c$ ($\tilde{w}$ stands for the vertical velocity component, and v_c and t_c are the characteristic velocity and time, respectively). This balance leads to $t_c \sim t_\mu \equiv \rho R^2/\mu$. In principle, the new equilibrium shape could be reached through either an

overdamped extensional deformation or the damping of free surface oscillations, depending on the relative magnitude of the viscous t_μ and capillary $t_\gamma \equiv (\rho R^3/\gamma)^{1/2}$ times. This latter characteristic time is determined from the balance between inertia and the characteristic capillary pressure σ/R, and establishes the scale of the oscillation period.

Figure 6 shows the temporal evolution of the apex position, $\widehat{Z}(t)$, of a subcritical drop. The solid line is the fit

$$\widehat{Z} = \widehat{Z}_0 + Ae^{-\alpha t}\cos(\omega t + \varphi) \tag{19}$$

to the experimental points. In Eq. (19), $\widehat{Z}_0$ is the apex equilibrium position, A is the initial amplitude of the oscillation, ω and γ are the oscillation frequency and damping rate, respectively, and φ is the phase. As can be observed, (19) fits remarkably well the experimental data over the entire drop evolution, which indicates that the drop oscillation approximately corresponds to a free oscillation mode from the instant at which the voltage is applied. This occurs because the initial amplitudes (damping rates) of other excited modes were much smaller (larger) than that of the mode observed in the experiment.

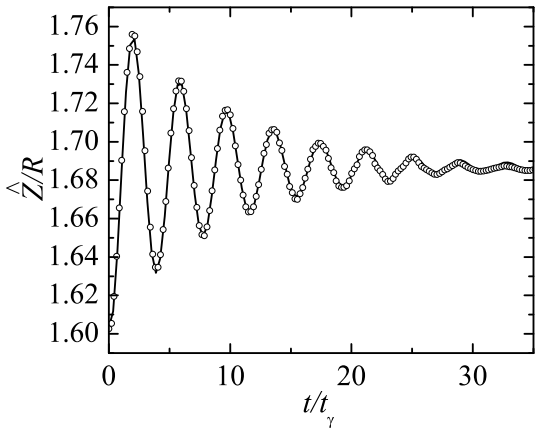

FIG. 6: Temporal evolution of the apex position $\widehat{Z}(t)$ for $\hat{\mathcal{V}} = 3.34$, $C = 0.0423$, $B = 1.20$, $B_e = 0.698$, and $\widehat{K} = 1642$. The symbols and solid line are the experimental results and the fit (19), respectively.

We also followed the fitting procedure described above to measure the damping rate and oscillation frequency in the simulations. Figure 7 shows the values of α and ω measured experimentally and calculated with the two numerical methods. The experimental and numerical values agree satisfactorily in all the cases considered. The fact that the perfect-conductor approximation provides accurate results indicates that the surface charge density

adapts "instantaneously" to the external electric field to screen it. As expected, the damping rate and the oscillation frequency scale as t_μ^{-1} and t_γ^{-1}, respectively ($t_\mu \simeq 0.37$ s and $t_\gamma \simeq 0.016$ s). The oscillation frequency decreases as the applied voltage (electric Bond number) approaches the critical value. Beyond that value, the drop stretches over a time interval of the order of the capillary time until it eventually breaks up. The behavior of subcritical electrified drops is similar to that of other purely mechanical systems[32,33], which can be explained in terms of the disparity between the electric $t_K \simeq 10^{-4}$ s and mechanical t_μ and t_γ characteristic times.

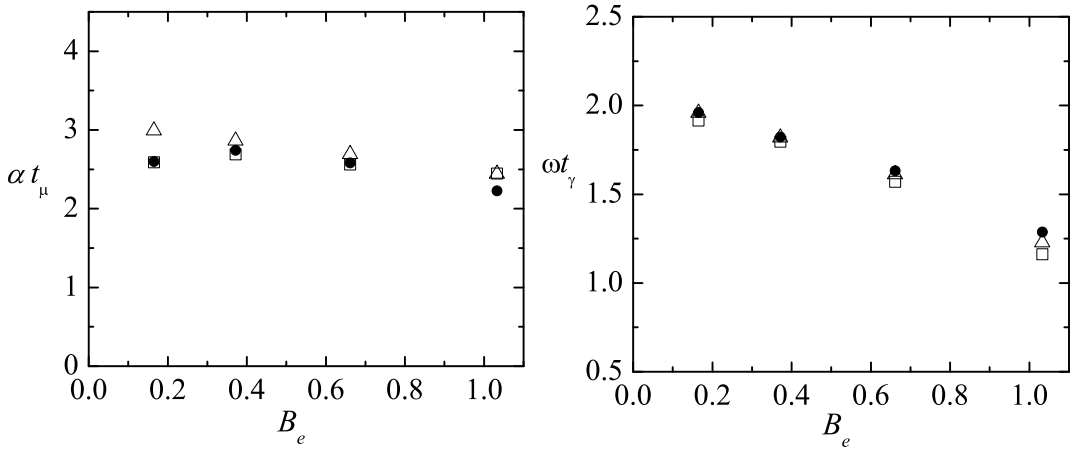

FIG. 7: Damping rate (left) and oscillation frequency (right) for $\hat{\mathcal{V}} = 3.34$, $C = 0.0423$, $B = 1.20$, and $\widehat{K} = 1642$. The circles, squares, and triangles correspond to the experimental results, the VoF method, and the spectral technique, respectively.

B. Supercritical drops

Figure 8 shows a sequence of images of a supercritical drop. One can distinguish two regimes: (i) the prejetting phase where the entire drop stretches under the action of the electric field [images (a)-(d)], and (ii) the jetting stage where a microjet is emitted from the tip of the deformed drop [images (e)-(h)]. The first regime is essentially the result of the competition between the electric pressure and surface tension, and takes place during a time interval of the order of the capillary time t_γ. Electric charge relaxation occurs on a time scale much shorter than that characteristic time, and thus the drop can be regarded as equipotential during this first regime. In the jetting regime, the shape of the drop tip

approaches the Taylor cone with a vertical semi-angle of 49.8°. A tip streaming appears in the drop apex before reaching that shape, giving rise to a charged jet of radius $R_j \simeq 20$ μm at the emission point (see Fig. 5d). The jet's size decreases downstream due to the action of electric stresses. The radius of the jet's front is estimated to be $R_f \simeq 10$ μm.

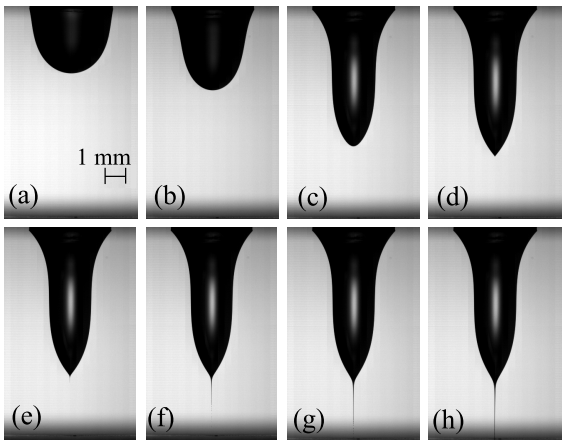

FIG. 8: Sequence of images of a supercritical drop evolution for $\hat{\mathcal{V}} = 3.26$, $C = 0.0431$, $B = 1.27$, $B_e = 2.74$, $\hat{K} = 1642$, and $t/t_\gamma = 0$ (a), 1 (b), 2.1 (c), 2.153 (d), 2.155 (e), 2.167 (f), 2.175 (g), and 2.186 (f).

In the experiment shown in Fig. 8, the inception of the tip streaming lasted less than the time interval $\delta t = 3.57 \times 10^{-5}$ s between the two consecutive images (d) and (e). The time on which tip streaming appeared was of the order of the *local* capillary time $t^*_\gamma \equiv (\rho R_j^3/\gamma)^{1/2} \simeq 1.6 \times 10^{-5}$ s (defined in terms of the jet's radius R_j), and smaller than the electric charge relaxation time $t_K \simeq 10^{-4}$ s. This means that electric charges could not move over the drop tip surface sufficiently fast to compensate for the increase of the surface tension in that region. The tension of the interface at the drop tip was relaxed by ejecting a liquid ligament[9]. Figure 9 shows a zoom of the images (d) and (e) displayed in Fig. 8. The dashed line in the left-hand image represents the Taylor cone. The tip streaming has just started at that instant, and it is already developed in the next image.

Figure 10 shows a comparison between the free surface positions measured in an experiment and calculated numerically for several instants of the prejetting regime. There is a satisfactory agreement between the experimental and theoretical results. The small deviations may be attributed to the differences between the experimental and numerical configurations. The solutions of the two numerical methods practically coincided, which

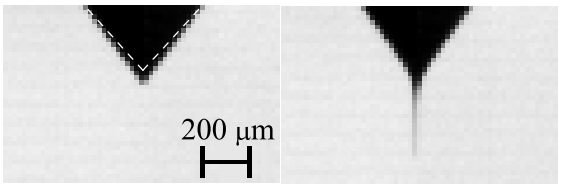

FIG. 9: Zoom of the images (d) (left-hand) and (e) (right-hand) displayed in Fig. 8. The dashed line in the left-hand image represents the Taylor cone.

shows that the perfect-conductor approximation provides accurate results for the prejetting regime.

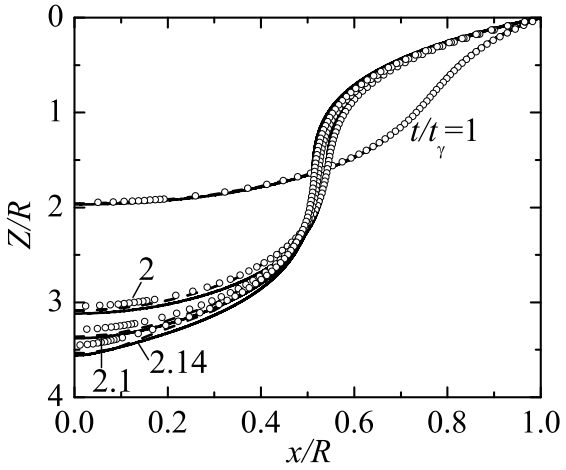

FIG. 10: Free surface position for $\hat{\mathcal{V}} = 3.26$, $C = 0.0431$, $B = 1.27$, $B_e = 2.74$, $\hat{K} = 1642$, and $t/t_\gamma = 1$, 2, 2.1, and 2.14. The symbols, solid lines, and dashed lines correspond to the experiments, the VoF method, and the spectral technique, respectively. The VoF and spectral method results were calculated for $B_e = 2.74$ and 2.61, respectively.

Figure 11 shows the temporal evolution of the apex position $\widehat{Z}$ for an applied voltage $V =$ 4000 V and two different volumes. The two theoretical approaches satisfactorily predict the apex position in the prejetting regime. As expected, the perfect-conductor approximation fails to describe the tip streaming leading to the microjet emission. Spurious results (not shown in the figure) were obtained with the spectral technique at the end of the prejetting regime owing to discretization errors. Even if those errors were eliminated, the perfect-conductor model would not yield tip streaming but the electrostatic Taylor solution[9]. The

leaky-dielectric model does predict the singular flow appearing at the drop tip. A video showing the temporal evolution of a drop as predicted by the VoF method and measured experimentally can be found as additional material. The parameters characterizing the fluid configuration are those of the case (b) in Fig. 11.

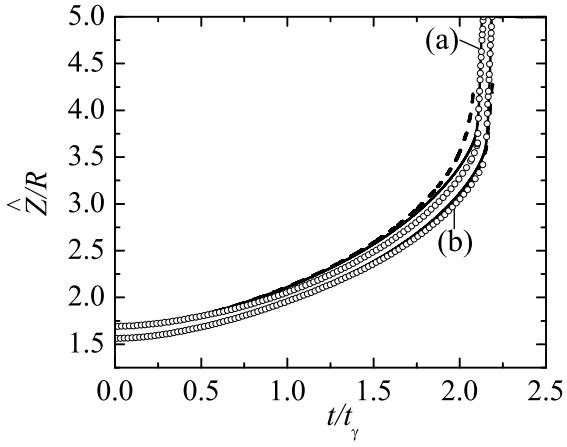

FIG. 11: Temporal evolution of the apex position $\widehat{Z}$ for $\{\hat{\mathcal{V}} = 3.54,\ C = 0.0425,\ B = 1.21,\ B_e = 2.67,\ \hat{K} = 1642\}$ (a) and $\{\hat{\mathcal{V}} = 3.26,\ C = 0.0431,\ B = 1.27,\ B_e = 2.74, \hat{K} = 1642\}$ (b). The symbols, solid lines, and dashed lines correspond to the experiments, the VoF method, and the spectral technique, respectively. The results of the VoF method were calculated for $B_e = 2.67$ (a) and 2.74 (b), while the spectral method predictions were obtained for $B_e = 2.53$ (a) and 2.61 (b).

The motion of the jet's front is shown in Fig. 12 for the same two cases considered in Fig. 11. The experimental results indicate that the jet's front velocity v_f increases during the inception of the tip streaming, and reaches an almost constant value about 5 m/s when this flow is developed. In this last stage, the order of magnitude of the flow rate $Q_f = v_f \pi R_f^2$ transported by the jet's front is 1 mm^3/s, the same as that of the capillary flow rate $Q_c = R_j^3/t_\gamma^*$. Interestingly, both Q_f and Q_c have the same order of magnitude as that of the characteristic flow rate $Q_0 = \gamma\varepsilon/(\rho K)$.[4] Therefore, Q_0 indicates the order of magnitude of the flow rate spontaneously adopted by the system, i.e., when this quantity is not imposed by any external means. The intrinsic flow rate Q_0 also indicates the order of magnitude of the minimum attainable flow rate in steady cone-jet mode of electrospray[5,21]. In fact, if the flow rate injected through the feeding capillary of electrospray were much smaller than Q_0, then the drop would loss volume and steady conditions could not be reached.

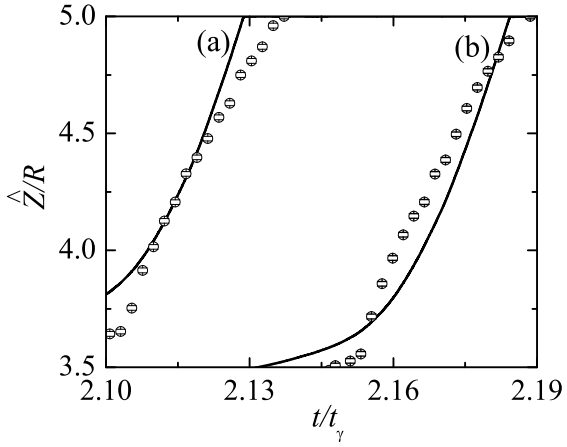

FIG. 12: Temporal evolution of the jet's front $\widehat{Z}$ for $\{\hat{\mathcal{V}} = 3.54,\ C = 0.0425,\ B = 1.21,\ B_e = 2.67,\ \hat{K} = 1642\}$ (a) and $\{\hat{\mathcal{V}} = 3.26,\ C = 0.0431,\ B = 1.27,\ B_e = 2.74, \hat{K} = 1642\}$ (b). The symbols and solid lines correspond to the experiments and the VoF method, respectively. The results of the VoF method were calculated for $B_e = 2.67$ (a) and 2.74 (b).

Figures 10-12 show that the leaky-dielectric model describes reasonably well the entire drop evolution in spite of the disparity between the spatial and temporal scales involved in the prejetting and jetting regimes[9]. Now, we proceed to analyze the features of the tip streaming flow from the numerical simulations of that model. Figure 13 shows the reduced pressure distribution along the symmetry axis in both the prejetting and jetting regimes. In the prejetting regime ($t/t_\gamma = 2.15$), a spherically symmetric flow driven by a favorable pressure gradient makes the liquid move towards the drop apex, where electric charges accumulate sufficiently fast to compensate for the surface tension. One can distinguish two flow regions in the jetting regime ($t/t_\gamma = 2.155$). In front of the meniscus tip ($z/R \lesssim 3.64$), the liquid motion is favored by the pressure gradient, which gives rise to parabolic-type velocity profiles (Fig. 14). The sign of the pressure gradient changes in the base of the emitted jet ($z/R \simeq 3.64$), and thus the liquid has to overcome an adverse pressure force beyond that point ($z/R \gtrsim 3.64$). Here, the flow is driven by the shear electric stress exerted on the interface by the axial component of the electric field[9]. For this reason, the interface velocity is larger than that of the bulk. The Reynolds number based on the interface radius takes small values in the two regions described above, and thus viscous diffusion of momentum practically flattens the velocity profiles.

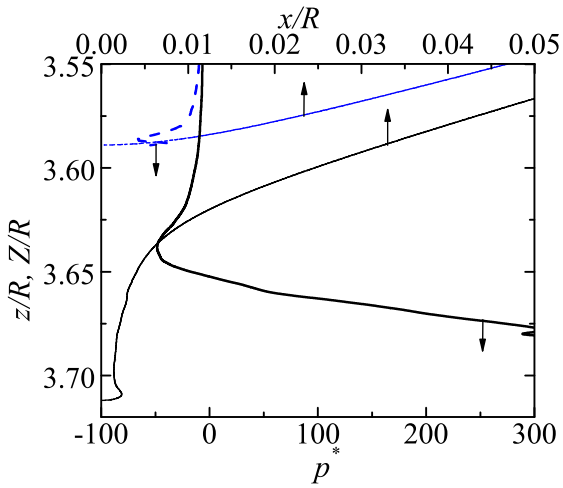

FIG. 13: (Color online) Gauge reduced pressure distribution $p^*(z) \equiv [p(z) - p(0)]/(\rho R^2/t_\gamma^2)$ along the symmetry axis and interface position $Z(x)$ both for $t/t_\gamma = 2.15$ (blue dashed lines) and 2.155 (black solid lines). The coordinate z is the vertical distance from the upper electrode. The dimensionless parameters characterizing the fluid configuration were $\hat{\mathcal{V}} = 3.26$, $C = 0.0431$, $B = 1.27$, $B_e = 2.74$, and $\hat{K} = 1642$.

Finally, the pressure distribution and the isocontours of the electric potential are plotted in Fig. 15 for the first stages of the tip streamming. Both the pressure and the electric potential are almost uniform in the prejetting regime. During the jet emission, one can distinguish the region of favorable pressure gradient (located in front of the meniscus tip) from the microjet, where the liquid has to overcome the pressure force.

VI. CONCLUSIONS

We studied both numerically and experimentally the electrohydrodynamic behavior of low-conductivity drops following high voltage switching. The leaky-dielectric and perfect-conductor models were solved with a VoF method and a spectral collocation technique, respectively. Also, we precisely measured the interface position with a sub-pixel resolution image processing technique. Both the simulations and the experiments showed that the drops oscillated for electric Bond numbers below a certain critical value, and emitted a microjet otherwise. The perfect-conductor model predicted reasonably well the damping rates and frequencies characterizing the oscillations of subcritical drops. This model also

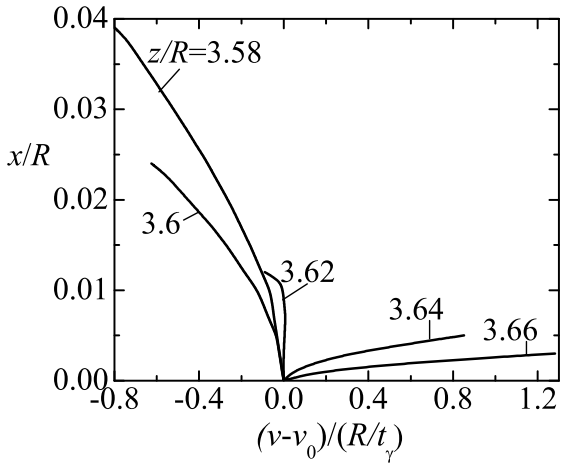

FIG. 14: Axial velocity profile $v(x)$ for $t/t_\gamma = 2.155$ over five streamwise sections as indicated by the levels. The coordinate z is the vertical distance from the upper electrode, while v_0 is the velocity at the symmetry axis. The dimensionless parameters characterizing the fluid configuration were the same as those of Fig. 13.

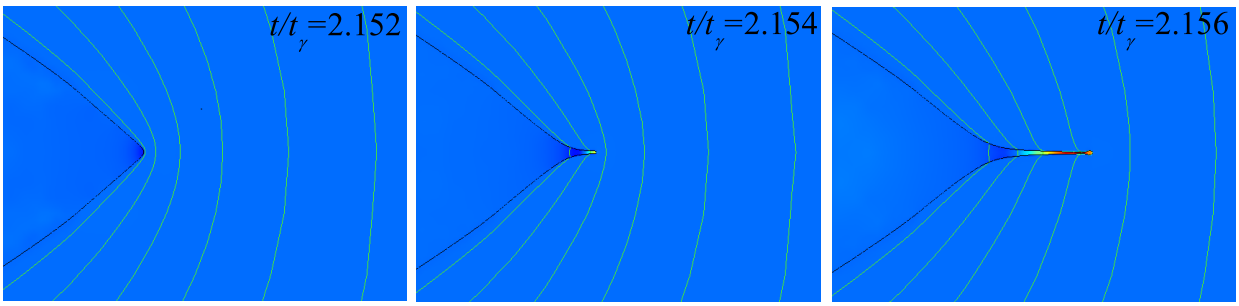

FIG. 15: (Color online) Pressure distribution for the first stages of the tip streamming. The dimensionless parameters characterizing the fluid configuration were the same as those of Fig. 13. The lines are isocontours of the electric potential.

provided satisfactory results for the prejetting regime in the supercritical case. We observed in the experiments that the inception of the jetting regime took place on a time scale much shorter than the electric relaxation time, which constitutes an experimental evidence of the numerical results of Collins *et al.*[9]. A good agreement between the leaky-dielectric model and the experiments was found for the drop-jet transitional region. Finally, the pressure and velocity fields in the transitional region were described from the simulations.

Partial support from the Ministry of Science and Education, Junta de Extremadura, and Junta de Andalucía (Spain) through Grants Nos. DPI2010-21103, GR10047, and P08-TEP-04128, respectively, is gratefully acknowledged.

---

[1] M. Cloupeau and B. Prunet-Foch, J. Aerosol Sci., **25**, 1021 (1994).

[2] I. Marginean, L. Parvin, L. Heffernan, and A. Vertes, Anal. Chem., **76**, 4202 (2004).

[3] J. Zeleny, Phys. Rev., **10**, 1 (1917).

[4] A. M. Gañán-Calvo, J. Fluid Mech., **507**, 203 (2004).

[5] J. F. de la Mora, Annu. Rev. Fluid Mech., **39**, 217 (2007).

[6] L. K. Lim, J. Hua, C.-H. Wang, and K. A. Smith, AICHE J., **57**, 57 (2011).

[7] D. A. Saville, Annu. Rev. Fluid Mech., **29**, 27 (1997).

[8] G. Taylor, Proc. R. Soc. Lond. A, **291**, 159 (1966).

[9] R. T. Collins, J. J. Jones, M. T. Harris, and O. A. Basaran, Nature Phys., **4**, 149 (2008).

[10] O. A. Basaran and L. E. Scriven, J. Colloid Interface Sci., **140**, 10 (1990).

[11] A. Bateni, S. S. Susnar, A. Amirfazli, and A. W. Neumann, Langmuir, **20**, 7589 (2004).

[12] J. Hua, L. K. Lim, and C.-H. Wang, Phys. Fluids, **20**, 113302 (2008).

[13] J. Feng and K. Beard, J. Fluid Mech., **227**, 429 (1991).

[14] S. B. Q. Tran, D. Byun, H. T. Yudistira, and J. H. Oh, Phys. Fluids, **23**, 022006 (2011).

[15] M. D. Paine, Microfluid Nanofluid, **6**, 775 (2009).

[16] I. Hayati, A. I. Bailey, and T. F. Tadros, J. Colloid Interface Sci., **117**, 202 (1987).

[17] P. K. Notz and O. A. Basaran, J. Colloid Interface Sci., **213**, 218 (1999).

[18] S. N. Reznik, A. L. Yarin, A. Theron, and E. Zussman, J. Fluid Mech., **516**, 349 (2004).

[19] S. N. Reznik, A. L. Yarin, E. Zussman, and L. Bercovici, Phys. Fluids, **18**, 062101 (2006).

[20] E. J. Vega, J. M. Montanero, and C. Ferrera, Measurement, **44**, 1300 (2011).

[21] M. A. Herrada, J. M. López-Herrera, A. M. Gañán-Calvo, E. J. Vega, J. M. Montanero, and S. Popinet, Phys. Rev. E, **86**, 026305 (2012).

[22] S. Popinet, J. Comput. Phys., **190**, 572 (2003).

[23] J. M. López-Herrera, S. Popinet, and M. A. Herrada, J. Comput. Phys., **230**, 1939 (2011).

[24] J. U. Brackbill, J. Comput. Phys., **100**, 335 (1992).

[25] J. F. Thompson, F. C. Thames, and C. M. Mastin, J. Comput. Phys., **47**, 1 (1982).

[26] M. R. Khorrami, Int. J. Numer. Methods Fluids, **12**, 825 (1991).

[27] M. G. Cabezas, A. Bateni, J. M. Montanero, and A. W. Neumann, Colloids Surf. A, **255**, 193 (2005).

[28] J. M. Montanero, C. Ferrera, and V. M. Shevtsova, Exp. Fluids, **45**, 1087 (2008).

[29] J. Canny, IEEE Trans. Pattern Anal. Mach. Intell., **8**, 679 (1986).

[30] B. Song and J. Springer, J. Colloid Interface Sci., **184**, 77 (1996).

[31] A. Savitzky and M. J. E. Golay, Anal. Chem., **36**, 1627 (1964).

[32] A. Prosperetti, J. Fluid Mech., **100**, 333 (1980).

[33] J. M. Montanero, Eur. J. Mech. B. Fluids, **22**, 167 (2003).